Non-Cartesian MR Angiography

Walter Block, PhD, Associate Professor,
Departments of Biomedical Engineering, Medical Physics, and Radiology,
University of Wisconsin-Madison, Madison, Wisconsin, USA

Oliver Wieben, PhD, Assistant Professor,
Departments of Medical Physics, Radiology, and Biomedical Engineering,
University of Wisconsin-Madison, Madison, Wisconsin, USA

1. Introduction

Magnetic Resonance Angiography has several compelling features including volumetric data acquisition and the availability of several contrast mechanisms. These can be used for imaging with and without exogenous contrast agents and to obtain anatomical as well as functional information, for example in the form of perfusion or velocity measurements. However, such MRA acquisitions require longer imaging times, which challenge scan completion without artifacts from physiological or involuntary patient motion, particularly for dynamic acquisitions such as bolus chasing, real-time imaging, or cardiac gated acquisitions.

The inherently 3D nature of MRI allows for fine depiction of vascular territories. However, as MR samples its data in an alternative Fourier domain, only a relatively few samples can be obtained at one time. If one desires to obtain a time-resolved depiction as injected contrast enhances the vasculature, a four dimensional space must be sampled. In one of the most demanding angiographic tasks, phase contrast angiography can obtain quantitative velocity data that is resolved to a spatial coordinate and a cardiac cycle. This imaging tasks requires four dimensional sampling (three spatial dimensions, time) of a vector quantity, the flow vector with three directional velocity components) constrained by physiological and clinical implementation limits. With such demanding acquisition requirements over so many dimensions, non-Cartesian trajectories have been developed to offer increased performance in MR angiography.

Non-Cartesian trajectories can offer increased performance in several ways, although not always simultaneously. Non-Cartesian methods can better utilize limited gradient hardware speed, improved the efficiency in which k-space is covered, decrease sensitivity to motion, and improve flow properties. Some non-Cartesian methods often offer a variable sampling trajectory where the center of k-space is sampled more often than higher spatial frequencies. These sampling patterns support time-resolved imaging in reconstruction methods that vary in performance, speed, accuracy, and complexity. In general, accuracy and performance generally improve with allowance for increases complexity and time within the reconstruction task.

Non-Cartesian methods offer possibilities to exploit the sparse nature of the vascular imaging task and the correlation between temporal frames in a time-resolved study. Vascular imaging differs from static imaging of many regions of the body in several important ways. Often vascular images are much more sparse than non-angiographic images of other parts of the body. The sparse nature of these images can be due to the high contrast provided by injected contrast agents. The ability to subtract out static signal, as in phase contrast imaging or through use of a pre-contrast mask, further increases the sparse nature of vascular images. In time-resolved imaging, significant correlation may exist between imaging frames and thus each image volume may not need to be acquired completely separately

The chapter first describes non-Cartesian acquisition and reconstruction theory, loosely classified as spiral and radial trajectories. A brief summary of methods being utilized to provide consistent performance with non-Cartesian methods is provided as these trajectories are generally less robust to several system and patient-induced imperfections than Cartesian methods. Methods that utilize non-Cartesian trajectories to improve time-resolved angiography are then discussed. Similar concepts used for accelerating time-resolved imaging can be used for quantitative resolve flow and perfusion throughout the cardiac cycle. Finally, trajectories with variable sampling densities are useful when using image estimation methods to increase performance. Here some form of *apriori* information is used to constrain the reconstruction process.

2. Non-Cartesian Trajectory Design

In MR imaging, data can be sampled in *k*-space on any 2D or 3D trajectory that the time-varying gradients and safety regulations regarding peripheral nerve and muscle stimulation and tissue heating can support. Although the first MR imaging method proposed the acquisition of projections (1), spin-warp imaging on a Cartesian sampling grid (2) became the predominantly used trajectory. The acquisition of data on such a rectilinear grid is fairly robust to inhomogeneities in the static magnetic field from imperfections in the system cause geometric distortions but little degradation of the point spread function (PSF).

In non–Cartesian acquisitions, these inhomogeneities introduce off-resonance effects which in turn cause blurring of the PSF. Advances in scanner hardware improved the field homogeneity and alternative sampling patterns with non–uniform sampling densities were revisited. Projection imaging (3) is a CT like acquisition where each echo represents a radial line traversing through the center of *k*-space. This method offers good suppression of motion artifacts and allows for imaging with very short echo times when the projections start in the center because they do not require any prewinding gradients. A disadvantage is the prolongation total imaging time because of the redundant oversampling of the central *k*-space region. *K*-space can be sampled with fewer echoes using spiral trajectories (4). Images can be acquired with as little as 30 to 40 echoes but this scheme is very sensitive to off-resonance effects. The sampling grids for these acquisitions schemes are shown in Figure 1.
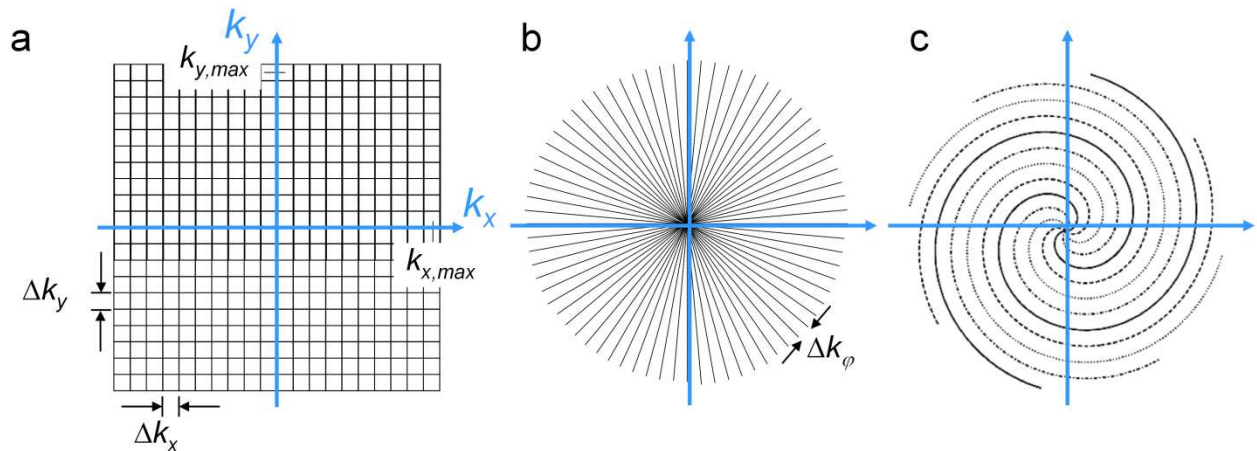

Figure 1 -   Strategies for 2D k-space sampling. Shown are the spin-warp (a), radial sampling (b), and interleaved spiral imaging (c) trajectory as examples for sampling patterns used in MR Angiography.

The trajectories can also be extended or combined into 3D acquisitions, for example for truly 3D radial, 3D spiral, cone, stack of spheres, shells trajectory, cones, and spiral PR. Hybrid 3D sampling patterns with non-Cartesain in plane encoding and traditional Fourier slice encoding have also been implemented,

predominantly for the sampling of imaging volumes of shorter dimensions in the through plane direction. More complete reviews of sampling patterns can be found elsewhere in the literature (5).
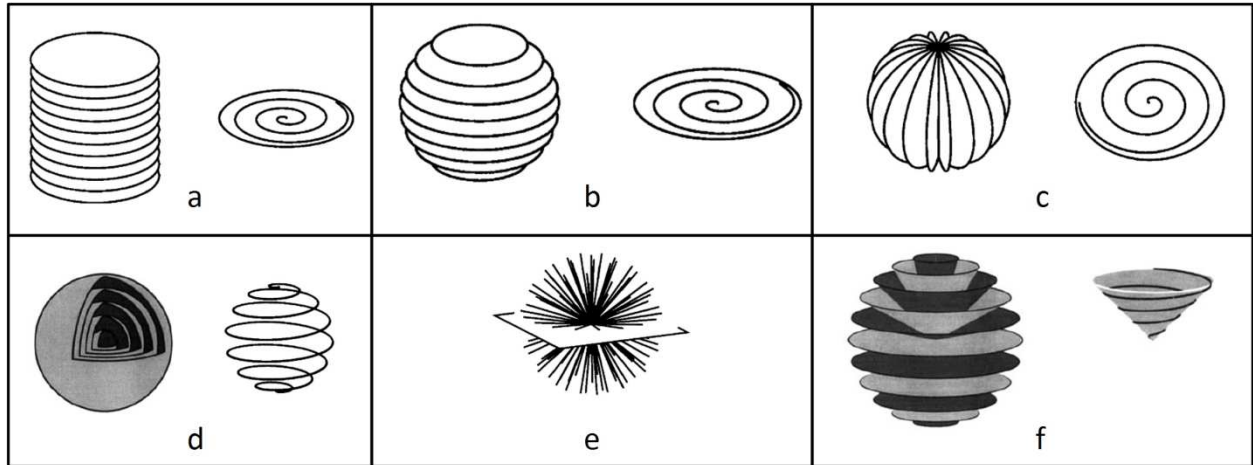

Figure 2 - *Strategies for 3D k-space sampling include cylindrical stack of spirals (a), spherical stack of spirals (b), a spiral-radial hybrid trajectory (c), concentric shells (d), a true 3D radial trajectory (e), and a stack of cones (f) (Figure adopted from P. Irarrazabal and D. G. Nishimura (5); reprinted with permission).*

2.1 General Considerations

2.1.1 Sampling Region

Sampling a cylinder of k-space saves 21.5% of the sampled space relative to a cube while sampling a sphere will save 47.6% of the required samples. While non-Cartesian trajectories can easily be tuned to cylindrical and spherical k-space regions, selection of phase-encoding and slice-encoding locations can achieve cylindrical sampling spaces.

2.1.2 Gradient Spoiling

As the readout direction is changing throughout a non-Cartesian scan, some attention has to be given to the method that spoil transverse signal in gradient-recalled sequences. Winding the magnetization to the same physical k-space location after each readout is generally a good way to remove variations in the transverse steady-state signal throughout the scan.

2.1.3 Field of View

In general, non-Cartesian trajectories are designed to sample along the readout direction at k-space intervals of 1/FOV as in Cartesian trajectories, where the FOV is the largest dimension of the acquired volume. Sampling along the readout dimension is constrained by the maximum slew rate achievable, and thus k-space sampling intervals often vary, especially at the beginning of the readout. Repetitions of the spiral or radial readout are then rotated in such a way to fill k-space. To provide full k-space sampling, enough repetitions of the model readout are needed such that the space of the interleaves is less than 1/FOV in all areas of k-space.

2.1.4 Off resonance

The extent of phase accrued by off-resonance spins during each readout is directly proportional to the readout duration. The amount of needed effort to remedy off-resonance effects thus increases with readout duration. The sophistication of any needed off-resonance processing depends also of course on

the amount of inhomogeneity present in the vascular territory of interest. While the appearance of off-resonance varies with trajectory, off-resonance effects are generally manifested by blurring and signal dropout in non-Cartesian trajectories.

2.1.5 Asymmetric FOVs

The largest spacing between k-space samples in the ensemble of readouts collected in the acquisition is usually designed to be no smaller than 1/FOV. The largest spacing may be designed to be 1/FOV for full sampling or greater than 1/FOV trajectories which one intentionally oversamples in regions of sparse and high contrast vasculature. Asymmetric FOVs that are tuned to certain vascular territory are generally easier to achieve with Cartesian trajectories than non-Cartesian methods, however non-Cartesian asymmetric FOVs are possible (6).
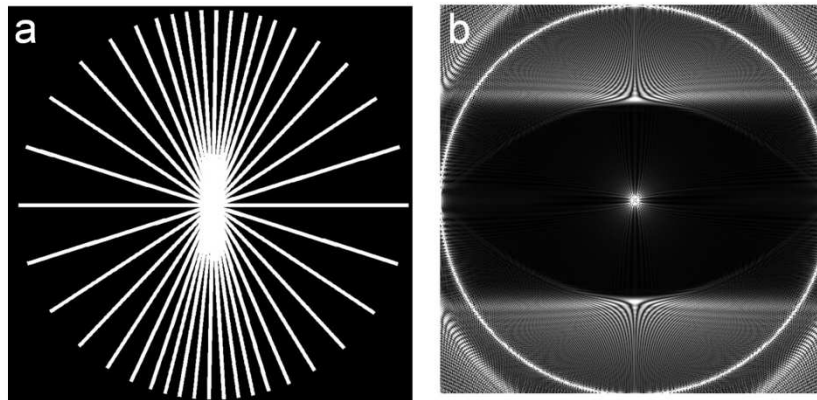

Figure 3 – Asymmetric FOV imaging with a radial trajectory with increased sampling density along the near vertical projections. This creates a larger horizontal FOV then vertical FOV (b). (Courtesy of Steve Kecskemeti, University of Wisconisn-Madison).

2.1.6 Flow Sensitivity

In general, trajectories whose first moment is small near the center of k-space have better flow properties(7). Trajectories for which the first moment changes smoothly as a function of k-space radius also are more robust in MR angiography. In general, trajectories which originate at the center of k-space without previous slice encoding will have more advantageous flow properties.

2.1.7 Sampling Density

The sampling density of radial trajectories varies significantly with k-space radius, falling off as $\frac{1}{k(r)}$ for 2D radial trajectories and $\frac{1}{k^2(r)}$ for true 3D radial trajectories. Sampling some spatial frequencies more often at the expense of others has liabilities when trying to cover all of k-space rapidly and has deleterious effects on SNR compared to flat sampling trajectories (8). Oversampling lower spatial frequencies had shown advantages for representing time-resolved imaging (9-11), motion artifact suppression, inherent field map and coil sensitivity generation, and constrained reconstruction methods (12-14).

In general, radial trajectories in MR angiography have emphasized the value of variable sampling density while working to deemphasize deleterious effects from an inefficient coverage of k-space. While their acquisition is less sophisticated than spiral trajectories, the short acquisition time required for each radial line or projection significantly limits off-resonance effects. Radial waveforms are generally easier to program in pulse sequences as well.

Spiral waveform design initially emphasized efficient, rapid k-space coverage with flat sampling density (5,15), where only a minimum portion of the waveform was slew-rate limited. Meyers presented an analytical expression to approximate the density of spirals (4) throughout their trajectory. Very simple methods that grid spiral data points to the nearest neighbor on an oversized Cartesian matrix have also been demonstrated (16) which simplify the density compensation computation. More recently, spiral design has incorporated variable sampling density to mitigate effects from aliasing from outside the FOV and to provide some of the advantages oversampling provides for representing time-resolved images volumes (17). The advantage of spiral acquisitions grow with longer readout duration, though these increase problems with off-resonance

The trajectories shown in first shown by Irarrazaval in Figure 2 have since been utilized in numerous examples of spiral MRA including these examples: stack of stars in the coronaries(18), cones in the peripheral vasculature (19), whole heart 3D radial imaging (20,21), and spiral projection imaging (22).

As an example, most 3D breath-hold coronary imaging can cover only a thin plane within the breath-hold requirement. In Figure 4 , a variable density spiral design is used to cover the entire heart with 0.8 x 0.8 x 1.6 mm resolution in just 17 heartbeats (23).

2.2 Spiral Trajectory Design

Although numerous implementations are possible, most spiral trajectories have been based on an Archimedes spiral. These trajectories follow the basis equation: $k(t) = \lambda\theta(t)e^{-i\theta(t)}$. The desired gradient waveforms are given by derivative of the k-space trajectory and scaled by the inverse of the gyromagnetic ratio. Linear functions of θ(t) lead to inefficient spirals with constant angular speed. The intuitive choice for efficient coverage of k-space would use a constant velocity spiral where $\theta(t) = \sqrt{t}$.

As this choice is not realizable in regions of the spiral where the slew-rate is limted, tradeoffs in the formulation of θ(t) between constant angular speed and constant velocity were formulated by Bornert *et al*.(24). While a more accurate solution for optimal use of gradient slew rate was formulated by King et al (25), this solution required significant computation. A closed form expression which produces images which are indiscernible from the optimal solution are provided by Glover et al. (26).

The complexity of spiral trajectory has created numerous strong publications where computational power is often used to create shorter trajectories, more accurate sampling density functions, and more powerful off-resonance correction methods. In many cases, simpler approximations can provide adequate performance for many vascular applications. A strong review of these tradeoffs is provided by Block and Frahm(27).
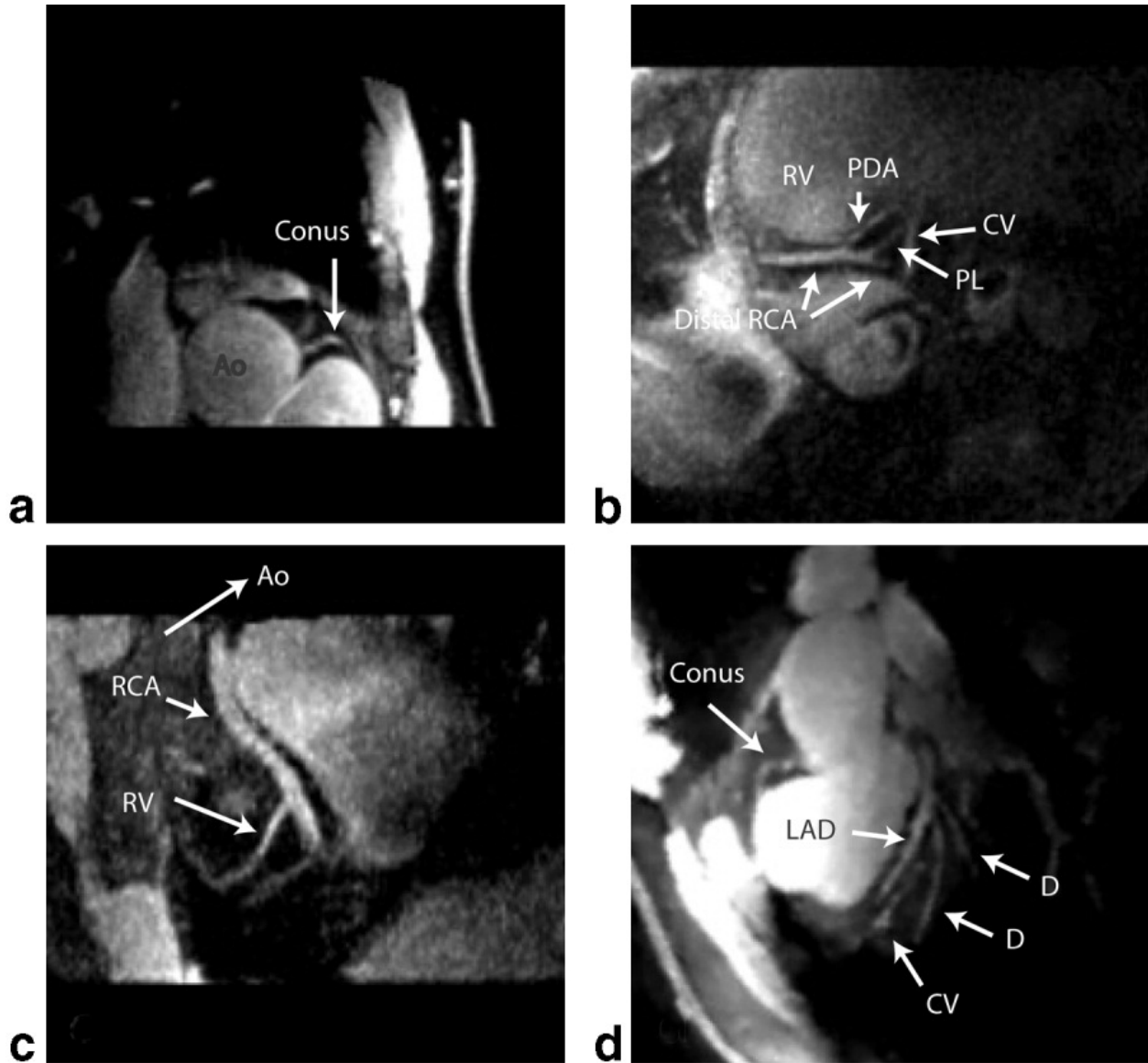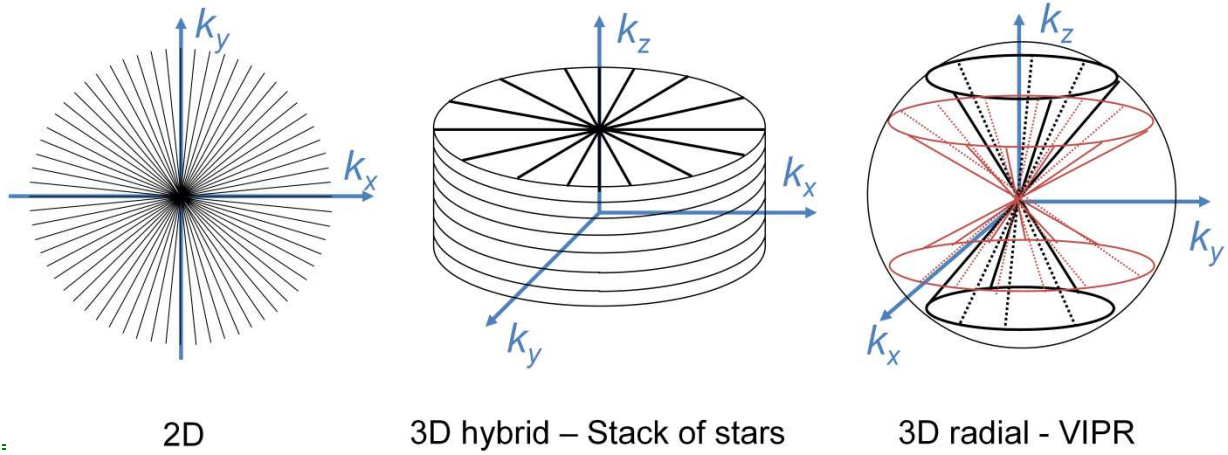
*Figure 4 – Detail of small coronary branches. Images **a-c** were acquired with a resolution 0.8 × 0.8 × 1.6 mm³. Image **d** was acquired with a resolution of 1 × 1 × 2 mm³ and reconstructed with the iterative algorithm. Image a shows a detail of the conus artery. The distal RCA including the posterior left ventricular artery (PL) and posterior descending artery (PDA) is displayed in image b. A lesser cardiac vein (CV) is also shown. Image c shows a detail of the mid to distal RCA with an acute marginal right ventricle (RV) branch. d: The mid LAD and diagonal branches. (Courtesy of J. Santos et al. (23); reprinted with permission).*

2.3 Projection Imaging

More specific aspects of the design of various radial trajectories and their effects on point spread functions are next provided.

| | 2D | 3D hybrid – Stack of stars | 3D radial - VIPR |

2.3.1 2D Projection Imaging

In 2D projection imaging, each readout traverses through the center of k-space. The sampling trajectory can be described in polar coordinates with a radial component k_r and an angle φ. A total of N_p repetitions are acquired with N_r samples and a sampling interval Δk_r along the readout direction. As the 1D Fourier transform of each repetition provides a projection of the object, the technique is also known a projection reconstruction (PR). The ensemble of transformed projections forms a sonogram, similar to computed tomography (CT) reconstruction, which can then be reconstructed with filtered backprojection.

Projection imaging, also known as radial sampling, leads to a non-uniform sampling density with emphasis on the low spatial frequencies. Let us consider the case where each projection starts at $-k_{r,\max}$, traverses through the origin, and ends at $+k_{r,\max}$ as shown in <u>Figure 5</u>~~Figure 6~~a. The radial sampling interval Δk_r supports an alias free reconstruction of distance $D = 1/\Delta k_r$ along the readout. The largest angular sampling distance $\Delta k_{\varphi,\max}$ occurs between adjacent spokes at the maximum sampled spatial frequency

$$\Delta k_{\varphi,\max} = \frac{\pi N_r}{2 N_p} \Delta k_r . \qquad \text{(Equ. 0.1)}$$

According to the Nyquist theorem, sampling with $\Delta k_{\varphi,\max} = \Delta k_r$ produces isotropic resolution over a radial FOV with a diameter D. This optimal sampling requires

$$N_{p,\text{opt}} = \frac{\pi}{2} N_r \qquad \text{(Equ. 0.2)}$$

projections. More projections do not provide better spatial resolution or a larger FOV while fewer projections reduce the artifact free FOV. In comparison, spin warp imaging requires only N_r readouts ($2/\pi = 63.7$ % less) for a squared FOV with identical resolution. This decrease in sampling efficiency is due to the oversampling of central k-space. It is important to note that any signal from outside the circular FOV does cause data inconsistencies in the projections and result in streak artifacts in the image. The

bandpass filter applied to the received signal does limit the signal contributions along the readout direction but not perpendicular to it.
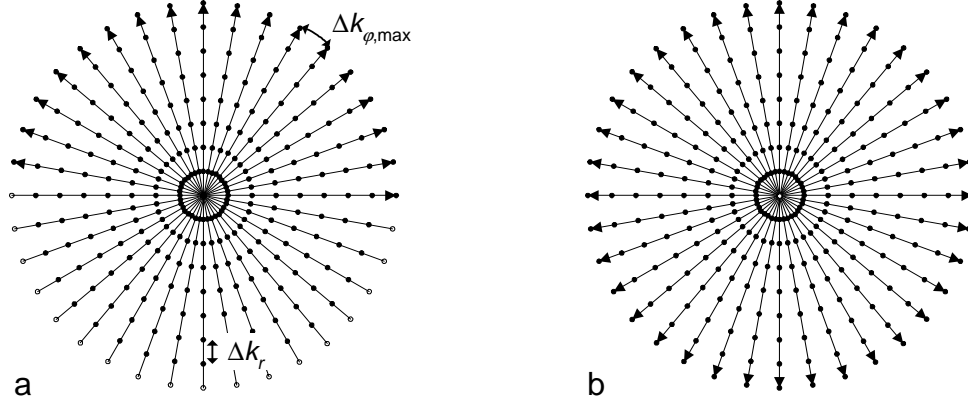

Figure 56 - Radial sampling schemes for projections from $-k_{r,max}$ to $+k_{r,max}$ (a) and from 0 to $+k_{r,max}$ (b). The starting point for each readout is shown as an unfilled circle and the endpoint with an arrow head. Both schemes are characterized by a constant radial sampling interval Δk_r and a maximum angular sampling interval $\Delta k_{\varphi,max}$.

While the repeated sampling of low spatial frequencies in each readout decreases the scan efficiency, radial sampling has very desirable properties for certain applications. Projection imaging is more robust to bulk motion because of the averaging effects from repeated sampling of the low spatial frequencies and more tolerable streak artifacts (3,28). This is also advantageous in diffusion weighted imaging where large gradients amplify artifacts from motion (28-30). The trajectory can be modified so that each projections starts in the *k*-space origin ($k_r = 0$) as shown in Figure 5Figure 6b. A free induction decay (FID) can then be acquired for the imaging of tissues with very short transverse relaxation times T_2, such as in the lungs (31,32). Projection imaging can also be advantageous to suppress displacement artifacts in flow imaging (7). Continuous and interleaved radial acquisitions were proposed for dynamic imaging in studies of the joints (33,34), catheter tracking in interventional MR (35,36), swallowing exams (37), and cardiac imaging (37). The properties of angular undersampling for faster imaging have been explored in various studies and will be discussed below.

2.3.2 Undersampled 2D Projection Imaging

If the number of projections is decreased below $N_{p,\mathrm{opt}}$ then the angular sampling interval $\Delta k_{\varphi,\mathrm{max}}$ exceeds the radial interval Δk_r and the high spatial frequencies are not sampled adequately. This leads to a reduced artifact free FOV (rFOV) with a diameter *d* given by the inverse of the largest sampling interval

$$ d = \frac{1}{\Delta k_{\varphi,\mathrm{max}}} = \frac{2N_p}{\pi \Delta k_r N_r} . \qquad \text{(Equ. 0.3)} $$
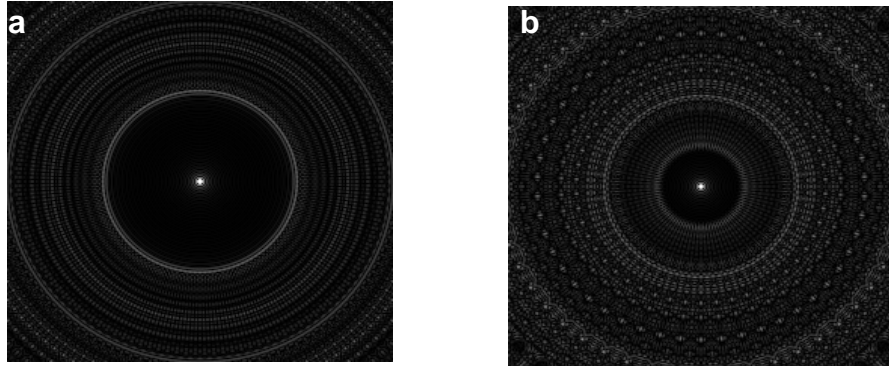
The ratio of the diameters of the reduced FOV and the full FOV is given by

$$ \frac{d}{D} = \frac{\Delta k_r}{\Delta k_{\varphi,\mathrm{max}}} = \frac{2}{\pi} \frac{N_p}{N_r} . \qquad \text{(Equ. 0.4)} $$

Figure 6

~~Figure 7~~ shows the point spread functions for a fully sampled radial trajectory ($N_p = \pi/2\ N_r$) and with a reduced number of projections ($N_p \ll \pi/2\ N_r$).

Figure 6~~7~~ - Radial sampling with adequate sampling ($N_p = \pi/2\ N_r$) results in a symmetric points spread function with an artifact free circular FOV inside the first lobe (a) up to $r = 1/\Delta k_r$. Angular undersampling causes streak artifacts outside a reduced FOV with smaller diameter as shown for an undersampling factor of 2.5 in (b) (Modeled after Scheffler and Hennig (38)).

As long as the imaged object does not extend outside the FOV, streak artifacts will only occur outside the reduced FOV and not interfere with the object generating the signal. In contrast to Cartesian acquisitions, where undersampling leads to coherent ghosts, undersampling creates a noise-like appearance. The property of spreading the artifact at a distance from the object is used for interventional MR with a large static FOV and a reduced dynamic FOV (38,39). In another approach, Shimizu et al. (40) purposefully undersampled at very high ratios to utilize the streaks for tracking the tip of a biopsy needle.

Peters et al. (41) first proposed the use of angularly undersampled projection reconstruction (PR) for large FOV imaging in MR Angiography using a hybrid trajectory with radial in-plane imaging and Fourier slice-encoding as shown in ~~Figure 5~~. They demonstrated that PR provides higher spatial resolution per unit time in high contrast environments where the number of imaged objects is limited. This is especially true in contrast-enhanced MRA. Here the streak artifacts from undersampling are often tolerable, leading to an increase in temporal resolution and/or spatial resolution, as shown in Figure 7~~Figure 8~~ The tradeoff becomes the occurrence of streak artifacts and a loss in SNR due to the shortened acquisition time, similar to parallel imaging..
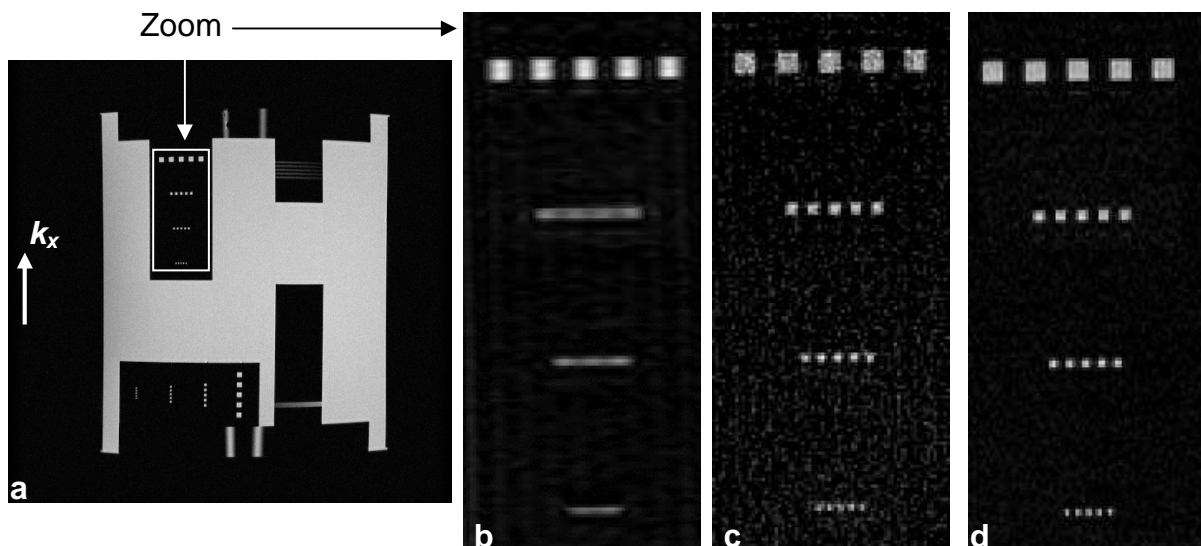
Figure 7~~8~~ - Resolution comparison between FT and PR from zoomed up regions of a phantom (a). All images were acquired with a readout length of 512 samples. The readout direction for the FT images is labeled k_x. Image (b) is acquired with 128 phase encodes on a Cartesian grid. Image (c) is a PR image from 128 projections acquired in the same scan time with increased spatial resolution in the phase encoding direction. Image (d) is sampled on a 512×512 Cartesian grid with a spatial resolution of 0.3×0.3 mm^2. The smallest dots in the image are 0.5 mm wide and spaced 0.5 mm apart. The undersampled PR image has a resolution similar to the 512×512 FT image, although it was acquired in one fourth of the time. Because of the shorter acquisition time, it also has a lower SNR. (Figure adopted from D. Peters et al. (41); reprinted with permission)

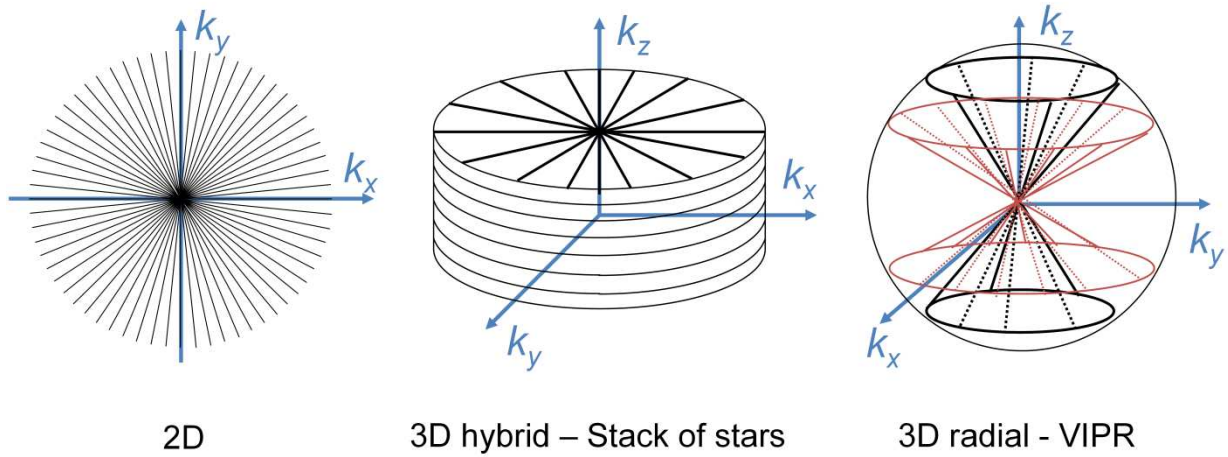### 2.3.3 3D Radial or Projection Imaging

2D   3D hybrid – Stack of stars   3D radial - VIPR

Figure 8~~5~~ - Hybrid 3D PR sequences use radial imaging in the through plane direction (left) and fully sampled Fourier encoding in the slice direction. This ensemble trajectory is often referred to as the stack of stars (middle). A truly 3D radial trajectory is shown at the right.

In a true 3D radial sequence as shown in ~~Figure 5~~c and with a corresponding pulse sequence in Figure 9, every projection lies in a sphere and traverses through the center of k-space in 3D radial acquisitions. Hence, this trajectory is best described in a spherical coordinate system with a radial component k_r, a polar angle θ, and an azimuthal angle φ. A total of N_p projections are acquired with N_r samples along the readout direction. The radial sampling interval Δk_r determines the spatial resolution and the diameter $D = 1/\Delta k_r$ of the maximum achievable artifact free spherical FOV. The Nyquist criterion is met if both angular sampling intervals are smaller than the radial sampling interval: Δk_φ, $\Delta k_\theta \leq \Delta k_r$. If we consider N_p evenly spaced projections ($\Delta k_\varphi = \Delta k_\theta = \Delta k$) that start at $-k_{max}$, traverse through the origin, and end at $+k_{max}$, then we can associate a surface area

$$A = \Delta k^2 = \frac{4\pi k_{max}^2}{2N_p} = \frac{2\pi}{N_p} k_{max}^2 \qquad \text{(Equ. 0.5)}$$

at k_{max} with each projection to cover the surface of the sampled sphere. The number of projections for optimal sampling ($\Delta k_\varphi = \Delta k_\theta = \Delta k_r = \Delta k$) is given by

$$N_{p,\text{opt}} = \frac{\pi}{2} N_r^2.$$ (Equ. 0.6)

This is $\pi/2 = 57\%$ more excitations than would be required for a cubic volume with identical spatial resolution with Fourier encoding. Because of this low sampling efficiency, Boada et al. (42) proposed a novel trajectory called TPI (twisted projection imaging) that starts as a radial projection until a certain radius when it switches to sample the surface of outwards pointing cone. This scheme provides the advantages of motion robustness and FID imaging with fewer projections.

2.3.4 Undersampled 3D Radial Imaging

By spreading the aliasing from undersampled energy from a 2D slice to a far larger 3D volume, the undersampling artifacts further diffuse into a structured background that resembles noise.   This technique, termed 3DPR or Vastly undersampled Isotropic PRojection (VIPR) imaging(10,43), provides isotropic resolution over large spherical fields of view.

Similar to the 2D case, undersampling leads to a reduced FOV, here a sphere with diameter $d = 1/\Delta k$. The ratio of the diameters for a reduced FOV and a full FOV is derived as

$$\frac{d}{D} = \frac{\Delta k_r}{\Delta k} = \sqrt{\frac{2}{\pi}} \frac{\sqrt{N_p}}{N_r}.$$ (Equ. 0.7)

The rFOV is proportional to the square root of the number of projections. Sparse sampling leads to artifacts from the undersampled high spatial frequencies and a reduced FOV around each object. The limiting factor in this acquisition is the decreased SNR and the artifacts introduced from undersampling.
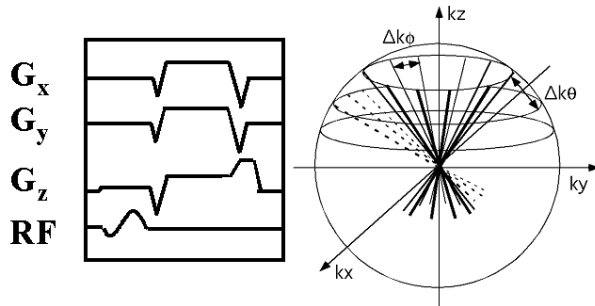
Figure 98 - Vastly undersampled Isotropic PRojection (VIPR) sequence (a) Timing diagram: The Gx,Gy, and Gz gradient amplitudes define the orientation of the partial diameter in the overall (b) k-space trajectory – Each excitation can cover one partial diameter as shown, a full diameter, or multiple diameters.

3. General Reconstruction of Non-Cartesian Acquisitions

In principle, there are many methods to reconstruct images from data acquired along non-Cartesian trajectories. In principle, methods that grid the acquired data onto a Cartesian grid are most utilized. With increases in computational power, parallel imaging, and model-based reconstruction, more complicated iterative algorithms are also creating increased attention. Prior to describing gridding, filtered backprojection for radial acquisitions is briefly discussed. A more thorough description of gridding is also provided in Bernstein's Handbook (44).

3.1 Filtered Backprojection

Filtered back projection (FBP) was developed for Computed Tomography and is an approximate implementation of the inverse Radon Transform. FBP is performed on sinogram data which are obtained by 1D Fourier transform of the radially acquired k-space data. Mathematically, the projections $p(r, \varphi)$ from an object distribution $f(x,y)$ are obtained as

$$p(r,\varphi) = \iint f(x,y)\,\delta(x\cos\varphi + y\sin\varphi - r)\,\mathrm{d}x\,\mathrm{d}y \qquad \text{(Equ. 0.1)}$$

In CT imaging, the projections are directly measured and in MRI the projections are obtained by an inverse 1D Fourier transform of each radial line along k_r.

$$p(r,\varphi) = \int P(k_r,\varphi)\,\mathrm{e}^{j2\pi k_r r}\,\mathrm{d}k_r \ . \qquad \text{(Equ. 0.2)}$$

The task then becomes the reconstruction of the backprojected image $f'(x,y)$. Since the sampling density in the center of k-space is much higher than at the edges, each projection has to be weighted with $|k_r|$ in k-space

$$P'(k_r,\varphi) = H(k_r)\,P(k_r,\varphi) = |\,k_r\,|\,P(k_r,\varphi), \qquad \text{(Equ. 0.3)}$$

where $H(k_r)$ is the filter for the projection and $H(k_r) = |k_r|$ is called the Ram–Lak filter. Unfiltered backprojection has been used in the early days of CT and results in the well known *star artifact*. The backprojected image can the be obtained as

$$f'(x,y) = \int_{0}^{\pi} \int_{-R}^{R} p'(r,\varphi)\,\delta(x\cos\varphi + y\sin\varphi - r)\,\mathrm{d}r\,\mathrm{d}\varphi \qquad \text{(Equ. 0.4)}$$

Different modifications to the Ram–Lak filter have been proposed for radial MR imaging. Pipe (45) discusses weighting options for the filter for noise reduction in undersampled data sets. Joseph (46) suggests to weight the central point $k_r = 0$ by the circular area it represents, $\pi\,\Delta k_r^2\,/\,4$, rather than setting it to zero.

Back-projecting magnitude data removes errors from variable delays imparted by eddy currents as the readout direction changes. While back-projecting magnitude data removes this problem, often the data in the body is inherently complex due to B0 inhomogeneity. Methods to remove the delays before back projection are preferable because then complex back-projection can be performed.

3.2 Reconstruction by Gridding

MR data acquired along non-Cartesian trajectories are generally reconstructed with a process known as gridding (47). If one represents M(k) as the continuous Fourier transform of the object magnetization m(x) and the k-space sample points as S(k), sampled data is represented as $M_s(\boldsymbol{k}) = M(\boldsymbol{k})S(\boldsymbol{k})$. Gridding interpolates the sampled MR data unto a Cartesian grid using a convolution kernel, C(k), after compensating for differences in sampling density, ρ(k), using the expression:

$$\left[M_c(k) = \left[\frac{M_s(\boldsymbol{k})}{\rho(\boldsymbol{k})} * C(\boldsymbol{k})\right] \cdot III(\boldsymbol{k})\right.$$

Several methods exist to compute the sampling density function ρ(k). A simple operation is simply $\rho(\boldsymbol{k}) = S(k) * C(\boldsymbol{k})$ while a more accurate iterative approach is given by Pipe (48) The reconstructed image volume is then

$$m_c(\boldsymbol{x}) = \frac{1}{c(\boldsymbol{x})} FTFT_{3D}^{-1}\big(M_c(\boldsymbol{k})\big)$$

where **x** describes the position in the object domain. The resultant image must be divided by the Fourier transform of the convolution kernel, as convolution in one domain results in multiplication in the other.

The choice of the interpolation kernel is ultimately a tradeoff between precision and speed and can have great impact on the reconstruction results (49). In general, good convolution kernels act over a quite localized region of k-space. As one tries to reduce error due to interpolation with wider kernels, the necessary time for interpolation grows rapidly. A simple and fast convolution kernel is the triangular window with a total width of two k-space samples. A popular kernel with more precise interpolation is the Kaiser–Bessel window. Dale et al. (50) introduced the use of a pre-calculated lookup table that allows for very rapid gridding in real-time applications. Gridding introduces some errors from the interpolation process but has been shown to produce images with better spatial resolution than filtered backprojection (51).

As sampling in one domain connotes replication in another, the choice of interpolation kernel also determines the amount of aliasing error one will suffer from adjacent image replicates in the image domain. In practice, this problem primarily affects tissue at the edge of the FOV. As vascular signal of interest is often not at the edges of the image, this problem is of less concern in vascular imaging. Intentionally gridding the data onto a finer grid artificially creates a larger FOV in which the replicates are further apart. Known as overgridding, this process reduces aliasing error. Though initially many overgridded by a factor of two, recent work with improved interpolation kernels demonstrates minimal error with overgridding factors as small as 1.25 (52). As an alternative to the computation involved in interpolating data onto a Cartesian gridding, it is possible to simply use nearest-neighbor interpolation with a significantly enlarged Cartesian k-space matrix (16).

3.3 Image Degradation due to K-Space Sampling Errors.

Effects of uncompensated system delays and eddy currents lead to sampling errors between the theoretical k-space sampling locations and actual k-space location. These errors manifest differently in images acquired using non-Cartesian methods relative to Cartesian trajectories. When using non-Cartesian trajectories, these effects lead to blurring, particularly as one moves away from the center of the image. These errors are much more benign in Cartesian imaging, as the errors are predominantly the same along each phase encoding acquisition. As sampling intervals become smaller with faster gradients, the size of delay that can create deleterious effects on image quality decreases. Furthermore, as these delays and eddy currents can change simply with gradient coil heating, measuring these errors quickly without a service procedure is essential for robust imaging. Correction methods to address these errors are discussed in the following sections.

3.3.1 Linear Eddy Current Correction

Multi-echo, echo-planar, and non-Cartesian trajectories place high demands on the gradient hardware, leading to increased induction of eddy currents. For conventional Cartesian acquisitions, these trajectory errors may be ignored as the resulting phase shift across the single readout direction is constant and does not appreciably affect image quality. This is not the case for multi-echo, EPI, and non-Cartesian trajectories, especially those employing bipolar readouts.

Methods to compensate these errors fall into two categories: system characterization and k-space measurement. System characterization methods model the gradient system as a linear system and then determine a modulation transfer function to relate the theoretical input waveforms and the actual

waveforms that are created. With the modulation transfer function, the actual k-space path can be predicted for any input trajectory. While elegant, these methods require long characterization times. The characterization may no longer hold after system upgrades, system maintenance, or even changes in the gradient coil temperature.

K-space measurement methods can be further broken down into methods that use numerous self-encoding pulses of different amplitudes prior to examining the readout gradient and methods that exploit localized signal. While the self-encoding methods have been proven to provide significant accuracy, they require multiple excitations and thus are rather time-consuming, often requiring minutes. Due to the limitations in speed provided by these methods, methods that exploit the phase of localized signal are gaining in interest.

By exciting a small slice off-isocenter and then subjecting that slice to the readout gradient under consideration, the entire test slice develops a phase which is the integral of the applied gradient field. The integral of course is proportional to the k-space trajectory. These measurements can be repeated on each physical gradient, or logical gradient if an oblique slice is being imaged. This method, suggested by Duyn *et al* (53), can be performed in only a few excitations and thus can be performed easily prior to each patient scan. The difference in actual k-space trajectory and the ideal trajectory can then be provided to the reconstruction. As the difference is primarily due to short time constant eddy currents generated by the gradients, the actual k-space deviation is linear with the amplitude of the readout waveform selected. Thus every waveform used during the scan need not be measured. If, for example, one readout gradient is calibrated for each axis, the k-space deviation present for scaled readout amplitudes on multiple axes is simply the scaled sum of the measured deviations on the individual gradient axes, each normalized for differences between the amplitude of the gradient using during the scan and the amplitude used during the calibration measurement.

For many commercial MR systems, the uncompensated eddy currents which effect image quality can be modeled primarily as short time constant which act as a delay. The difference between a nominal and delayed waveform will appear similar to the derivative of k-space, or as the gradient waveform itself. In Figure 10, a common 1,-2,1 gradient pulse used in multiple echo radial imaging is analyzed. The k-space deviations are significant, but note that majority of the deviation can be modeled as a delay. Likewise, Robinson et al. (22) studied the delays in refocusing along spiral waveforms and found changes of only fractions of a microsecond as the spiral grew in amplitude. This is logical, as there may be some non-linear effects occurring in the hardware as the slew requirements decrease at higher amplitudes.
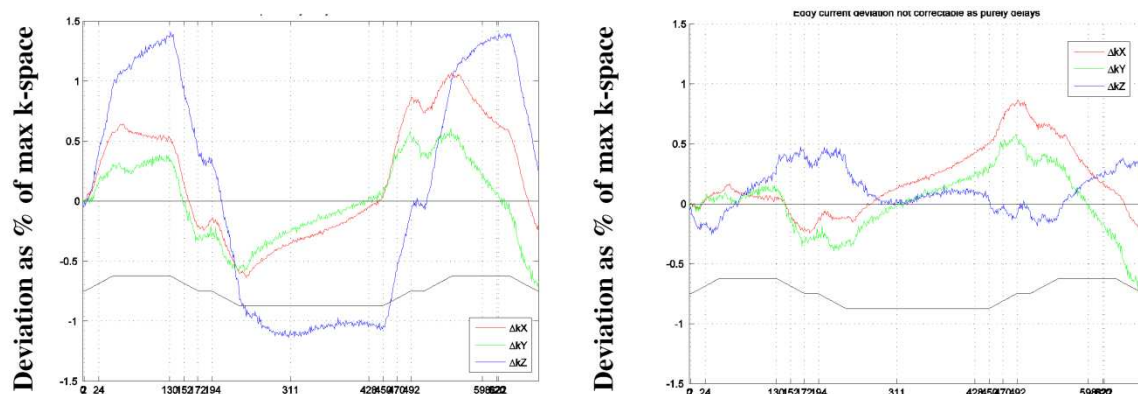
Deviation: Delay + remaining errors   **Deviation: Remaining errors only**

Figure 10- K-space deviation for 1,-2,-1 gradient pulse (black waveform) is shown for each physical axis (left). Notice that much of the deviation appears similar to the gradient waveform itself, and thus the deviation can be

modeled as a delay. After removing the portion of the deviation that can be modeled as delay, much smaller deviations are remaining and primarily affect larger spatial frequencies.

In practice with this method, a traditional slice select gradient is used to select the spins at a known position, D_r, from isocenter. Note that the slice thickness should be small relative to D_r. The phase of the acquired signal is obtained and unwrapped. Choosing a slice somewhat near to isocenter will greatly simplify unwrapping the phase of the obtained signal, as this reduces the slope of the phase. Subtracting the phase accrued by simply exciting the slice and acquiring the signal with no readout gradient will remove any unwanted phase due to B0 inhomogeneity. Scaling this phase measurement by $1/D_r$. provides the actual k-space trajectory for the gradient under test. This measurement is repeated for each of the three logical axes.

Note the magnitude of the calibration signal is actually mapping out the k-space representation of the slice profile. Thus an RF profile that is thinner than the acquired readout resolution is helpful to remove zeros in the magnitude of the calibration signal where the phase will be indeterminate. Adding a frequency dephaser prior to the measurement can also mitigate this problem(54). Care must also be taken in off-axis imaging, such as the breast or peripheral vasculature to assure that slices in locations covered by the coils used during the exam are excited for the calibration.

3.3.2 Off-Axis Imaging

Timing errors in the hardware demodulator may lead to phase errors if one uses real-time frequency demodulation to center at a location off-isocenter. The easiest way to mitigate this problem, if you can increase your data acquisition rate, is to avoid using the real-time frequency demodulation featue and do all demodulation during reconstruction. This solution has consequence of increasing your raw data file size also.

To simplify phase unwrapping in the Duyn method when one is forced to use a slice far off-isocenter to generates signal, one can acquire phase information on two slices centered a short distance on either side from the off-center image center. Real-time frequency demodulation can be performed for the image volume center during the measurement. The phase difference between these two slices is unaffected by demodulator timing errors, thus ensuring accurate *k*-space trajectory measurements with simple phase unwrapping.

If one cannot simply increase the receiver bandwidth an image as if you are at isocenter, then one must take care to account for these errors. The real-time frequency demodulation signal,

$$\Delta f(t) = \gamma(G_x(t)d_x + G_y(t)d_y + G_z(t)d_z) \qquad \text{(Equation 1.2)}$$

used to center the image at a position d_x, d_y, d_z is based on the nominal gradient waveforms and thus nominal *k*-space locations, marked by (+) signs in Figure 1.3. Figure 1.3 graphically describes the sources of phase errors in non-Cartesian imaging. When there is a timing discrepancy between the real-time frequency demodulation hardware and the receiver, the effective demodulation can be modeled as being based on a delayed *k*-space trajectory along the nominal trajectory, marked by (□). However, the optimal frequency demodulation signal would be based on the actual *k*-space locations, marked by (o), which are altered due to anisotropic delays and eddy currents.
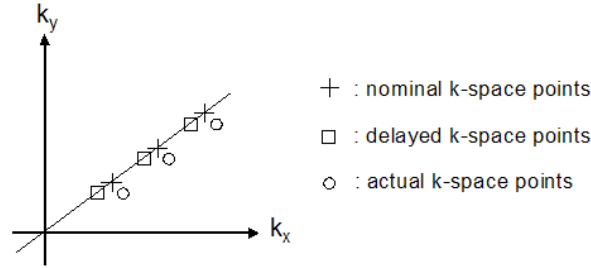
Figure 11 - Location of the nominal k-space sample points are marked by (+). Fast gradient characterization determines the actual locations (o). Due to timing errors between the frequency demodulation hardware and the receiver, the scanner creates a demodulation reference signal based on a delayed nominal trajectory (□). Proper gridding and correction of the phase error between the phase demodulation signal required at the actual k-space points (o) and the phase applied by the scanner hardware (□) provides consistent image quality.

The delay between the actual and the nominal real-time frequency demodulation can be determined quickly (55). Simply excite a slice and impart real-time frequency demodulation on it while playing no gradients. The difference between the actual phase accrual and the nominal accrual will indicate the delay

4. Time-averaged Imaging with Radial Trajectories

Steady-state free precession (SSFP) rapidly creates high signal with T2-like contrast with bright fluid signal which can be utilized for non-contrast-enhanced angiography. However, SSFP also produces bright fat signal which may interfere with visualization of the vasculature. Methods exist to exploit the differing phase of fat and water spins in SSFP sequences, but they require tight constraints ranging from 2.4 ms at 1.5T (56) to 3.6 ms at 1.5T and 3T(57). When utilized with a Cartesian trajectory, much of the TR time is spent prewinding and rewinding the spins rather than obtaining spatial encoding information. Radial sequences can be utilized to efficiently sample k-space on and out and back trajectory that eliminates the wasted time spent preparing and restoring magnetization in Cartesian trajectories. The pulse sequence, trajectory, and sample images of the peripheral vasculature obtained with 0.29 mm isotropic resolution are shown in Figure 12Figure 12.

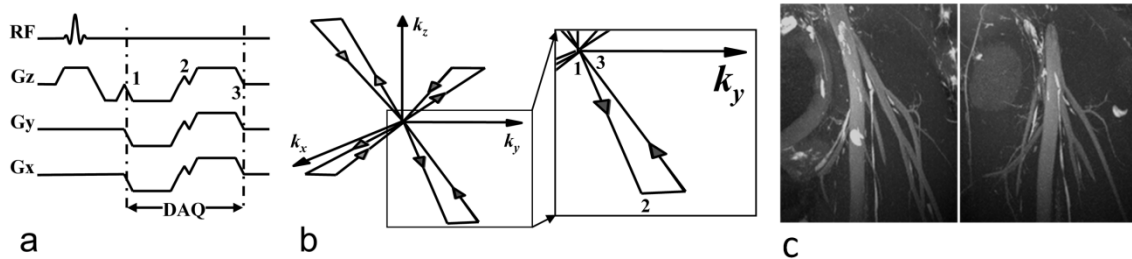*Figure 12 - Dual half-echo 3D radial pulse sequence (a) and k-space trajectory that efficiently uses the available TR duration for spatial encoding. b) Two radial lines, each one half of a diameter, are sampled per TR. c) Oblique MIPs of the vasculature in the knee joint acquired with 0.29 mm isotropic resolution using trajectory in shown in b)*

The inherent oversampling of the center of *k*-space in this radial acquisition results in signal averaging that reduces motion artifact at the expense of slightly increased blurring (44). This principle is demonstrated in Figure 13 , where respiratory triggering but no ECG gating is used to acquire a non-

contrast-enhanced angiogram of the thoracic vasculature with a 3D radial trajectory. Similar acquisitions with a Cartesian trajectory would require ECG gating to properly depict the ascending aorta (58).
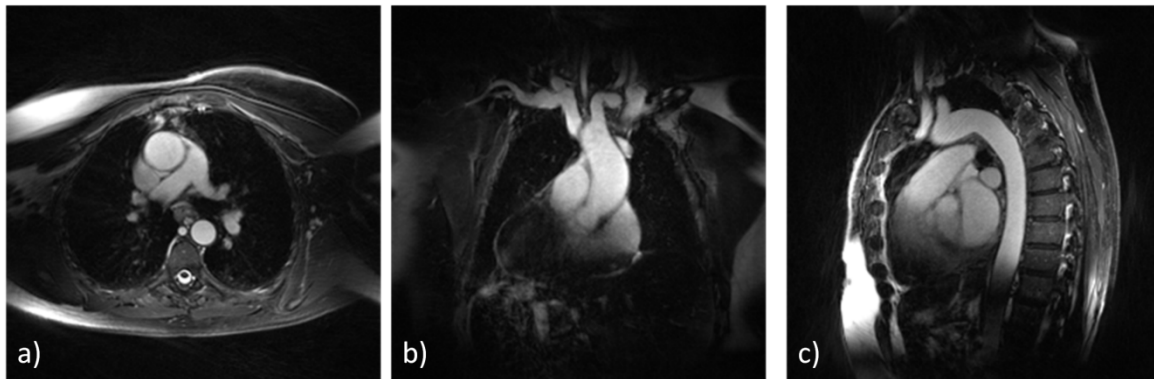

Figure 13 - 3D radial trajectory with fat/water separation is used to assess a suspected aortic aneurysm in this patient using a non-contrast-enhanced steady-state acquisition with fat/water separation. Inherent motion suppression allows a clear depiction of the ascending aorta without ECG gating.

In Figure 12~~Figure 12~~ and Figure 13, a prime benefit of the radial trajectory is effective spatial encoding. The static imaging environment in the periphery and the use of respiratory triggering in the thorax allows for longer scan times which minimize undersampling. In the next section, undersampling in sparse vascular environments using non-Cartesian trajectories is described.

5. Time-resolved MRA

Achieving a time-resolved image series by simply acquiring the same set of k-space samples at each time point is the simplest method for 4D imaging, but it also fails to exploit the significant correlation of the image volumes between time frames. Only a relatively small percentage of an imaging volume contain vascular signal while the larger amounts of static tissue are intentionally suppressed in MRA. Radial and interleaved k-space trajectories provide a basis to exploit these characteristics to improve performance of time-resolved MRA.
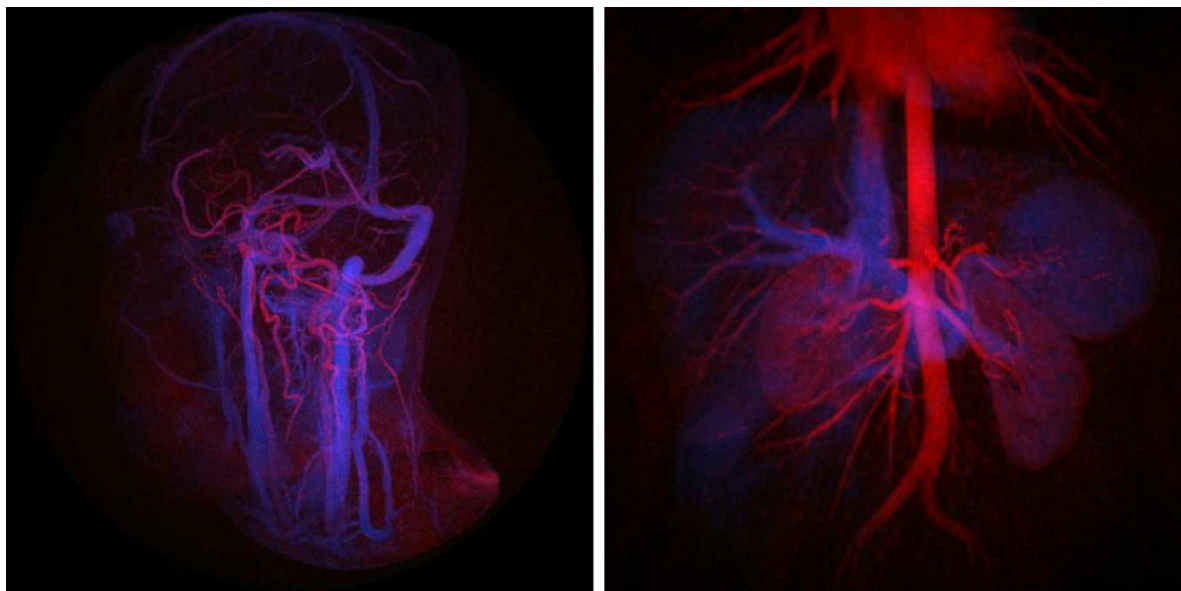
5.1 Temporal Processing

The oversampling of the center of k-space with radial methods can be exploited in time-resolved MRA to depict temporal enhancement during a contrast injection or resolve flow throughout the cardiac cycle(59). The projection acquisition order can be subdivided into interleaved sets so that spatial frequency orientations throughout k-space are sampled on an interval less than or equal to the desired frame rate. A sliding window reconstruction technique with a temporal aperture that widens for k-space points acquired at larger radii is utilized (10,11,60-63). The aperture widens at higher spatial frequencies to diminish the penalty from aliased, unsampled energy. These methods provide an additional order of magnitude in acceleration, though it should be noted that the acceleration factor is maximized at lower spatial frequencies and decreases for higher spatial frequencies.

The k-space weighted imaged contrast (KWIC) method first was developed to sample the center of k-space at different points in a T2 recovery curve(61). Only a small number of radial experiments at the desired echo time were needed to characterize the center of k-space, which dominates the visualization of image contrast, especially for larger objects. As the k-space radius grew, data from an increasing aperture of acquisition points along the recovery curve is utilized. The KWIC concept can be easily extended to replace the recovery dimension with a temporal dimension for CE-MRA or perfusion imaging (11,64).

Here, one data set can be filtered multiple times to produce a set of time-resolved images. At a desired time point, data from only a limited number of radial projections is used at the center of k-space. Larger annuli of k-space require data taken over a larger time interval to fill the space. The KWIC method has been utilized for dynamic imaging of the breast, lung, and liver(11,65) in the assessment of perfusion when characterizing lesions.

The process of creating temporal weighting with KWIC can be viewed as a density compensation problem in which different density compensation functions are generated for each reconstructed time point. If one views the different compensation functions as time progresses, the filter has an appearance like that of a moving tornado and is thus sometimes referred to as a tornado filter. A general, deterministic algorithm to generate temporal filters for variable density k-space acquisitions is provided by Liu *et al*(62). The method allows more flexibility in selecting the temporal weighting of data at the center of k-space and properly calculates the density compensation function for more complicated trajectories, such as those using ramp sampling. The use of these types of tornado filters to depict the enhancement patterns throughout the body is depicted in Figure 14Figure 14.

Figure 14-Time-resolved CE-MRA using 3D radial acquisitions and temporal filtering are utilized for head and neck (left) and abdominal study (right) where a post-processing algorithm renders early enhancing vessels red and later enhancing vessels as blue.

6. Quantitative Velocity Imaging Using 3D Radial Trajectories

MR Angiography can not only provide morphological information such as the patency of vessels, but also quantitative flow measurements with velocity sensitive encoding techniques. Phase contrast (PC) MRI, is commonly used in clinical applications such as the evaluation of valve disease. However, the extensive scan time for PC MR acquisitions have limited their use to one directional velocity mapping of a single slice to be completed in a single breath hold.

Only recent advances in MR hardware design, particularly more powerful gradient systems and the use of parallel imaging techniques have permitted the use of three directional PC MR with volumetric coverage in broader human studies because of the extensive scan time associated with multi-directional velocity encoding, respiratory and cardiac gating, and volumetric acquisitions. These studies have mainly focused on the largest vessel in the human body, the aorta, because of the necessary compromises in spatial resolution to limit the scan time to below 15-20 min (66).

PC MRA with alternative trajectories, such as 3D radial sampling with PC VIPR (67) allow for significant data undersampling because of the data sparsity from the inherent subtraction process in the reconstruction, thereby providing high signal from the vessels and only small contributions from the background signal. In addition, view sharing like techniques within the cardiac cycle can be applied for additional significant savings in scan time. The obtained high spatial resolution in clinically feasible scan times and advantageous properties in respect to motion suppression makes PC VIPR a viable alternative for high resolution MR Angiography in patients in which the standard contrast enhanced MR angiography (CE MRA) is contraindicated due to risk associated with nephrogenic systemic fibrosis (NSF) (68) and improves the ability to quantify velocity and flow parameters as well as hemodynamic derivatives, such as relative pressures (59), pulse wave velocities, and wall shear stress.

To reliably achieve high quality images, several correction schemes are applied to account for the effects of T1-saturation, trajectory errors, motion, and aliasing associated with undersampling. A dual echo acquisition as shown in Figure 15 can be used to derive a field map and reduce off resonance effects with a computationally more demanding reconstruction process (69). Trajectory errors are compensated for in the gridding process by independently mapping out trajectory derivations for the radial readout gradients as well as the bipolar gradients in x, y, and z. This is accomplished with a short calibration routine using the Duyn method (53) and using the principle of superposition for the indivudal combinations of projection angles and flow encoding gradients.
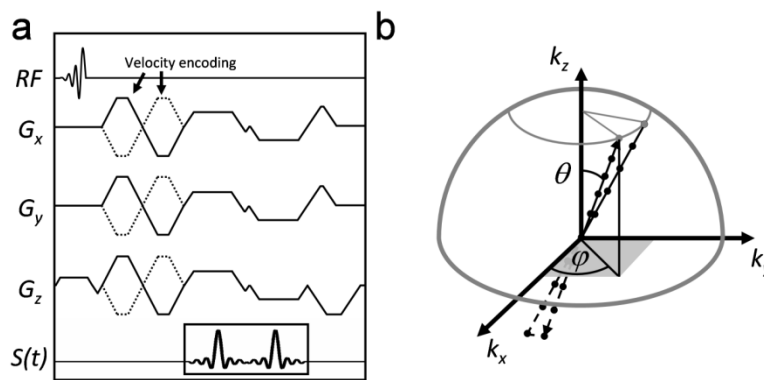

Figure 15 – The dual echo PC VIPR pulse sequence (a) and k-space trajectory (b). Velocity encoding is achieved with the use of a standard bipolar gradients superimposed onto the prewinders along the direction of velocity encoding. Acquisitions with reversed bipolar gradients are used for the removal of phase contributions that are not contributed to motion.

Ultimately, the phase contrast data are reconstructed as magnitude images, velocity vector fields, and angiograms calculated similar to complex difference images and additional post-processing is applied to derive hemodynamic parameters from the velocity fields. Advanced visualization software can be used to interactively display the volumetric, cine velocity vector fields, possibly in combination with superimposed vascular anatomy as shown in Figure 16Figure 16. However, these displays require significant post-processing since no such software packages dedicated to medical imaging currently exists.
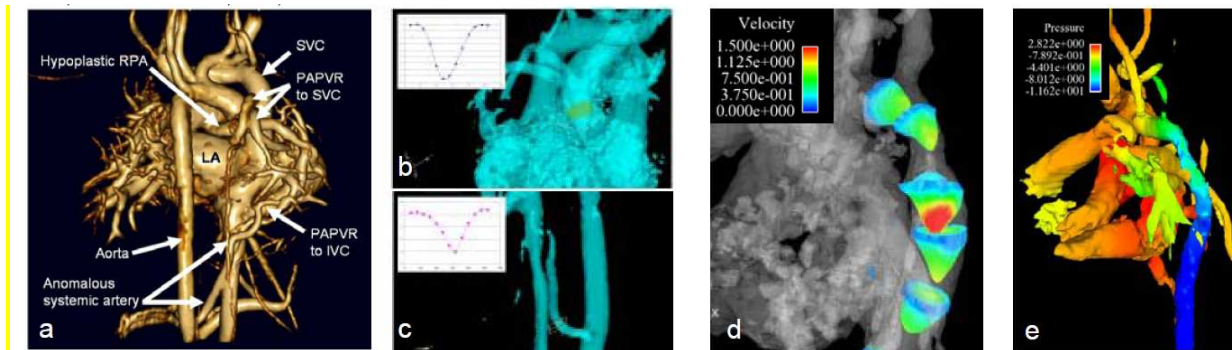
Figure 16 – PC VIPR exam of a 18 month-old male with pulmonary venolobar syndrome consisting of a hypoplastic right pulmonary artery (RPA), partial anomalous pulmonary venous return (PAPVR) to superior vena cava (SVC) and inferior vena cava (IVC), and an anomalous systemic pulmonary artery from the abdominal aorta to the right lower lobe. LA, left atrium. The non-contrast enhanced MR angiogram (a) shows a posterior view from volume rendered PC VIPR data. Flow-time curves were measured at different locations using advanced visualization software, here in the ascending aorta (b) and anomalous systemic artery (c). With such 4D MR flow imaging, measurements can be made in any arbitrary orientation after the images have been acquired. (d+e) Hemodynamic analysis for a patient with aortic coarctation. (d) Flow velocity profiles showing the highest velocity immediately distal to the coarctation. (e) Pressure difference map showing the drop over the coarctation.

7. Advanced Temporal Processing

Newer reconstruction methods aim to speed time-resolved imaging by undersampling while using other information to limit undersampling artifacts. In general, these image estimation methods require sparsity in some domain. These methods include a family of methods that use a high SNR image with little temporal resolution to constrain an image reconstruction using a limited amount of temporal data, known as HIghly constrained back Projection (HYPR)(70) and HYPR Local Reconstruction (HYPR LR) (13). These single pass methods are generally rapid, but their accuracy can vary with the sparsity of the object. Improved accuracy can be achieved with iterative reconstruction methods such as IHYPR (71) or conjugate gradient HYPR (72). The relation of these methods to compressed sensing is developed in Lustig *et al.* (14). Here the requirements for sparsity are more general. For example, sparsity can be present in the actual image itself, the derivative of the image, or the wavelet representation of the image.

1.   Lauterbur PC. Image formations by induced local interactions: Examples employing nuclear magnetic resonance. Nature 1973;242:190-191.
2.   Edelstein WA, Hutchison JM, Johnson G, Redpath T. Spin warp NMR imaging and applications to human whole-body imaging. Physics in Medicine & Biology 1980;25(4):751-756.
3.   Glover GH, Pauly JM. Projection reconstruction techniques for reduction of motion effects in MRI. Magnetic Resonance in Medicine 1992;28(2):275-289.
4.   Meyer CH, Hu BS, Nishimura DG, Macovski A. Fast spiral coronary artery imaging. Magn Reson Med 1992;28(2):202-213.
5.   Irarrazabal P, Nishimura DG. Fast three dimensional magnetic resonance imaging. Magnetic Resonance in Medicine 1995;33(5):656-662.
6.   Larson PE, Nishimura D. Variable Field-of-View Three-Dimensional Projection-Reconstruction Imaging. 2007; Berlin. p 417.
7.   Nishimura DG, Jackson JI, Pauly JM. On the nature and reduction of the displacement artifact in flow images. Magn Reson Med 1991;22(2):481-492.
8.   Tsai CM, Nishimura DG. Reduced aliasing artifacts using variable-density k-space sampling trajectories. Magn Reson Med 2000;43(3):452-458.
9.   Korosec FR, Frayne R, Grist TM, Mistretta CA. Time-resolved contrast-enhanced 3D MR angiography. Magn Reson Med 1996;36(3):345-351.

10. Barger AV, Block WF, Toropov Y, Grist TM, Mistretta CA. Time-resolved contrast-enhanced imaging with isotropic resolution and broad coverage using an undersampled 3D projection trajectory. Magnetic Resonance in Medicine 2002;48(2):297-305.

11. Song HK, Dougherty L. Dynamic MRI with projection reconstruction and KWIC processing for simultaneous high spatial and temporal resolution. Magn Reson Med 2004;52(4):815-824.

12. Mistretta CA, Wieben O, Velikina J, Block W, Perry J, Wu Y, Johnson K. Highly constrained backprojection for time-resolved MRI. Magn Reson Med 2006;55(1):30-40.

13. Johnson KM, Velikina J, Wu Y, Kecskemeti S, Wieben O, Mistretta CA. Improved waveform fidelity using local HYPR reconstruction (HYPR LR). Magn Reson Med 2008;59(3):456-462.

14. Lustig M, Donoho D, Pauly JM. Sparse MRI: The application of compressed sensing for rapid MR imaging. Magn Reson Med 2007;58(6):1182-1195.

15. Meyer CH, Hu BS, Nishimura DG, Macovski A. Fast spiral coronary artery imaging. Magn Reson Med 1992;28(2):202-213.

16. Oesterle C, Markl M, Strecker R, Kraemer FM, Hennig J. Spiral reconstruction by regridding to a large rectilinear matrix: a practical solution for routine systems. J Magn Reson Imaging 1999;10(1):84-92.

17. Tsai CM, Nishimura DG. Reduced aliasing artifacts using variable-density k-space sampling trajectories. Magn Reson Med 2000;43(3):452-458.

18. Thedens DR, Irarrazaval P, Sachs TS, Meyer CH, Nishimura DG. Fast magnetic resonance coronary angiography with a three-dimensional stack of spirals trajectory. Magn Reson Med 1999;41(6):1170-1179.

19. Gurney PT, Hargreaves BA, Nishimura DG. Design and analysis of a practical 3D cones trajectory. Magn Reson Med 2006;55(3):575-582.

20. Stehning C, Bornert P, Nehrke K, Eggers H, Stuber M. Free-breathing whole-heart coronary MRA with 3D radial SSFP and self-navigated image reconstruction. Magn Reson Med 2005;54(2):476-480.

21. Holmqvist MH, Cao J, Hernandez-Pineda R, Jacobson MD, Carroll KI, Sung MA, Betty M, Ge P, Gilbride KJ, Brown ME, Jurman ME, Lawson D, Silos-Santiago I, Xie Y, Covarrubias M, Rhodes KJ, Distefano PS, An WF. Elimination of fast inactivation in Kv4 A-type potassium channels by an auxiliary subunit domain. Proc Natl Acad Sci U S A 2002;99(2):1035-1040.

22. Blatter DD, Parker DL, Robison RO. Cerebral MR angiography with multiple overlapping thin slab acquisition. Part I. Quantitative analysis of vessel visibility. Radiology 1991;179(3):805-811.

23. Santos JM, Cunningham CH, Lustig M, Hargreaves BA, Hu BS, Nishimura DG, Pauly JM. Single breath-hold whole-heart MRA using variable-density spirals at 3T. Magn Reson Med 2006;55(2):371-379.

24. Bornert P, Schomberg H, Aldefeld B, Groen J. Improvements in spiral MR imaging. Magma 1999;9(1-2):29-41.

25. King KF, Foo TK, Crawford CR. Optimized gradient waveforms for spiral scanning. Magn Reson Med 1995;34(2):156-160.

26. Glover GH. Simple analytic spiral K-space algorithm. Magn Reson Med 1999;42(2):412-415.

27. Block KT, Frahm J. Spiral imaging: a critical appraisal. J Magn Reson Imaging 2005;21(6):657-668.

28. Gmitro AF, Alexander AL. Use of a projection reconstruction method to decrease motion sensitivity in diffusion-weighted MRI. Magnetic Resonance in Medicine 1993;29(6):835-838.

29. Jung KJ, Cho ZH. Reduction of flow artifacts in NMR diffusion imaging using view-angle tilted line-integral projection reconstruction. Magn Reson Med 1991;19(2):349-360.

30. Trouard TP, Theilmann RJ, Altbach MI, Gmitro AF. High-resolution diffusion imaging with DIFRAD-FSE (diffusion-weighted radial acquisition of data with fast spin-echo) MRI. Magnetic Resonance in Medicine 1999;42(1):11-18.

31. Bergin CJ, Pauly JM, Macovski A. Lung parenchyma: projection reconstruction MR imaging. Radiology 1991;179(3):777-781.

32. Gewalt SL, Glover GH, Hedlund LW, Cofer GP, MacFall JR, Johnson GA. MR microscopy of the rat lung using projection reconstruction. Magnetic Resonance in Medicine 1993;29(1):99-106.
33. Rasche V, de Boer RW, Holz D, Proksa R. Continuous radial data acquisition for dynamic MRI. Magnetic Resonance in Medicine 1995;34(5):754-761.
34. Rasche V, Holz D, Proksa R. MR fluoroscopy using projection reconstruction multi-gradient-echo (prMGE) MRI. Magnetic Resonance in Medicine 1999;42(2):324-334.
35. Rasche V, Holz D, Kohler J, Proksa R, Roschmann P. Catheter tracking using continuous radial MRI. Magn Reson Med 1997;37(6):963-968.
36. Shankaranarayanan A, Wendt M, Aschoff AJ, Lewin JS, Duerk JL. Radial keyhole sequences for low field projection reconstruction interventional MRI. J Magn Reson Imaging 2001;13(1):142-151.
37. Rasche V, Proksa R, Sinkus R, Bornert P, Eggers H. Resampling of data between arbitrary grids using convolution interpolation. IEEE Transactions on Medical Imaging 1999;18(5):385-392.
38. Scheffler K, Hennig J. Reduced circular field-of-view imaging. Magnetic Resonance in Medicine 1998;40(3):474-480.
39. Weiss S, Rasche V. Projection-reconstruction reduces FOV imaging. Magn Reson Imaging 1999;17(4):517-525.
40. Shimizu K, Mulkern RV, Oshio K, Panych LP, Yoo SS, Kikinis R, Jolesz FA. Rapid tip tracking with MRI by a limited projection reconstruction technique. Journal of Magnetic Resonance Imaging 1998;8(1):262-264.
41. Peters DC, Korosec FR, Grist TM, Block WF, Holden JE, Vigen KK, Mistretta CA. Undersampled projection reconstruction applied to MR angiography. Magnetic Resonance in Medicine 2000;43(1):91-101.
42. Boada FE, Gillen JS, Shen GX, Chang SY, Thulborn KR. Fast three dimensional sodium imaging. Magnetic Resonance in Medicine 1997;37(5):706-715.
43. Glover GH, Pauly JM. Projection reconstruction techniques for reduction of motion effects in MRI. Magn Reson Med 1992;28(2):275-289.
44. Bernstein MA, King KF, Zhou ZJ. Handbook of MRI pulse sequences. Amsterdam ; Boston: Academic Press; 2004. xxii,1017 p. p.
45. Pipe JG. Reconstructing MR images from undersampled data: data-weighting considerations. Magn Reson Med 2000;43(6):867-875.
46. Joseph PM. Sampling errors in projection reconstruction MRI. Magnetic Resonance in Medicine 1998;40(3):460-466.
47. O'Sullivan J. A fast sinc function gridding algorithm for Fourier inversion in computer tomography. IEEE Trans Med Imaging 1985;M1:200.
48. Pipe JG, Menon P. Sampling density compensation in MRI: rationale and an iterative numerical solution. Magnetic Resonance in Medicine 1999;41(1):179-186.
49. Jackson J, Meyer C, Nishimura D. Selection of a convolution function for Fourier inversion using gridding. IEEE Trans Med Imaging 1991;10:473-478.
50. Dale B, Wendt M, Duerk JL. A rapid look-up table method for reconstructing MR images from arbitrary K-space trajectories. IEEE Trans Med Imaging 2001;20(3):207-217.
51. Lauzon ML, Rutt BK. Polar sampling in k-space: Reconstruction effects. Magnetic Resonance in Medicine 1998;40(5):769-782.
52. Beatty PJ, Nishimura DG, Pauly JM. Rapid gridding reconstruction with a minimal oversampling ratio. IEEE Trans Med Imaging 2005;24(6):799-808.
53. Duyn JH, Yang Y, Frank JA, van der Veen JW. Simple correction method for k-space trajectory deviations in MRI. J Magn Reson 1998;132(1):150-153.
54. Beaumont M, Lamalle L, Segebarth C, Barbier EL. Improved k-space trajectory measurement with signal shifting. Magn Reson Med 2007;58(1):200-205.

55. Jung Y, Jashnani Y, Kijowski R, Block WF. Consistent non-cartesian off-axis MRI quality: calibrating and removing multiple sources of demodulation phase errors. Magn Reson Med 2007;57(1):206-212.
56. Vasanawala SS, Pauly JM, Nishimura DG. Linear combination steady-state free precession MRI. Magn Reson Med 2000;43(1):82-90.
57. Leupold J, Hennig J, Scheffler K. Alternating repetition time balanced steady state free precession. Magn Reson Med 2006;55(3):557-565.
58. Groves EM, Bireley W, Dill K, Carroll TJ, Carr JC. Quantitative analysis of ECG-gated high-resolution contrast-enhanced MR angiography of the thoracic aorta. AJR Am J Roentgenol 2007;188(2):522-528.
59. Lum DP, Johnson KM, Paul RK, Turk AS, Consigny DW, Grinde JR, Mistretta CA, Grist TM. Transstenotic pressure gradients: measurement in swine--retrospectively ECG-gated 3D phase-contrast MR angiography versus endovascular pressure-sensing guidewires. Radiology 2007;245(3):751-760.
60. Pipe JG. Reconstructing MR images from undersampled data: data-weighting considerations. Magn Reson Med 2000;43(6):867-875.
61. Song HK, Dougherty L. k-space weighted image contrast (KWIC) for contrast manipulation in projection reconstruction MRI. Magn Reson Med 2000;44(6):825-832.
62. Liu J, Redmond MJ, Brodsky EK, Alexander AL, Lu A, Thornton FJ, Schulte MJ, Grist TM, Pipe JG, Block WF. Generation and visualization of four-dimensional MR angiography data using an undersampled 3-D projection trajectory. IEEE Trans Med Imaging 2006;25(2):148-157.
63. Lai P, Huang F, Li Y, Nielles-Vallespin S, Bi X, Jerecic R, Li D. Contrast-kinetics-resolved whole-heart coronary MRA using 3DPR. Magn Reson Med 2010;63(4):970-978.
64. Song HK, Dougherty L, Schnall MD. Simultaneous acquisition of multiple resolution images for dynamic contrast enhanced imaging of the breast. Magn Reson Med 2001;46(3):503-509.
65. Lin W, Guo J, Rosen MA, Song HK. Respiratory motion-compensated radial dynamic contrast-enhanced (DCE)-MRI of chest and abdominal lesions. Magn Reson Med 2008;60(5):1135-1146.
66. Wigstrom L, Sjoqvist L, Wranne B. Temporally resolved 3D phase-contrast imaging. Magn Reson Med 1996;36(5):800-803.
67. Gu T, Korosec FR, Block WF, Fain SB, Turk Q, Lum D, Zhou Y, Grist TM, Haughton V, Mistretta CA. PC VIPR: a high-speed 3D phase-contrast method for flow quantification and high-resolution angiography. AJNR Am J Neuroradiol 2005;26(4):743-749.
68. Thomsen HS, Morcos SK, Dawson P. Is there a causal relation between the administration of gadolinium based contrast media and the development of nephrogenic systemic fibrosis (NSF)? Clin Radiol 2006;61(11):905-906.
69. Johnson KM, Lum DP, Turski PA, Block WF, Mistretta CA, Wieben O. Improved 3D phase contrast MRI with off-resonance corrected dual echo VIPR. Magn Reson Med 2008;60(6):1329-1336.
70. Mistretta CA, Wieben O, Velikina J, Block W, Perry J, Wu Y, Johnson K, Wu Y. Highly constrained backprojection for time-resolved MRI. Magn Reson Med 2006;55(1):30-40.
71. O'Halloran RL, Wen Z, Holmes JH, Fain SB. Iterative projection reconstruction of time-resolved images using highly-constrained back-projection (HYPR). Magn Reson Med 2008;59(1):132-139.
72. Griswold MA. More optimal HYPR reconstruction using a combination of HYPR and conjugate-gradient minimization. 2007; Joint Annual Meeting ISMRM-ESMRMB - Berlin. p 834.